

# An improved model for malaria pigment and $\beta$ -hematin: Fe(OEP)picrate

Ratchadaporn Puntharod,<sup>a</sup> Kenneth J. Haller,<sup>b\*</sup>  Evan G. Robertson,<sup>c</sup>  
Eunice S. H. Gwee,<sup>d</sup> Ekaterina I. Izgorodina<sup>d</sup> and Bayden R. Wood<sup>d\*</sup> 

Synthesis and crystallographic and spectroscopic structural characterization, along with spectral band assignments calculated by using density functional theory (M06L/cc-pVDZ and B3LYP/6-31G(d)), are reported for Fe(OEP)picrate as a model for hemozoin (malaria pigment) and its synthetic analog  $\beta$ -hematin, which are spectroscopically identical. The average Fe–N distance, 2.044 (12) Å, and the Raman modes indicate a high-spin five-coordinate iron(III) complex. Resonance enhancement is observed for the totally symmetric oxidation state marker band  $\nu_4$  along with the characteristic bands of  $C_\beta$ -substituted hemes in the ranges of 1621–1639  $\text{cm}^{-1}$  for  $\nu_{\text{as}}(C_\alpha C_m)$  and 750–756  $\text{cm}^{-1}$  for  $\nu(\text{pyr breathing})$  similar to  $\beta$ -hematin and hemozoin when using near-IR excitation wavelengths. The similarity of the resonance Raman spectral profiles for Fe(OEP)picrate and  $\beta$ -hematin, along with the structural results, indicates that Fe(OEP)picrate is an excellent model for understanding the stereochemistry and intermolecular interaction of  $\beta$ -hematin. Copyright © 2017 John Wiley & Sons, Ltd.

## Introduction

Strategies for antimalarial drug design aim at producing effective, nontoxic, and inexpensive agents for use against malaria in the developing world, where the combined mortality rate is over one million per year with some 300–500 million people afflicted with the disease.<sup>[1]</sup> Most deaths occur in children under 5 years of age, and child mortality from cerebral malaria is ~20%.<sup>[2]</sup> Of the children that survive malaria, 10% are left with severe neurological defects affecting their education and long-term employment prospects.<sup>[2]</sup> Moreover, ineffective treatments can result in anemia and low birth weight<sup>[3]</sup> compromising the health of children and adults infected with *Plasmodium falciparum* or *Plasmodium vivax* and making them more susceptible to other infections.<sup>[4]</sup> During the intra-erythrocytic phase of the malaria parasite's life cycle, the parasite can consume up to 75% of an infected cell's hemoglobin, releasing toxic free heme, which can kill the parasite by disrupting cell membranes. Malaria parasites have evolved a detoxification method, which results in the formation of an inert crystallized heme aggregate known as hemozoin (Hmz). Hmz has a spectroscopically identical synthetic analog known as  $\beta$ -hematin ( $\beta$ -H).<sup>[5]</sup> The structure of  $\beta$ -H has been interpreted from powder synchrotron X-ray diffraction data to be an array of dimers linked through reciprocal iron–carboxylate bonds to one of the propionate side chains, with the dimers, in turn, linked by hydrogen bonds.<sup>[6]</sup> At least two models have been proposed to explain how quinine-based antimalarial drugs such as chloroquine and amodiaquine inhibit heme aggregation. Crystal structure data of  $\beta$ -H indicate that chloroquine absorbs onto the Hmz surface, resulting in inhibition of further heme aggregation.<sup>[6]</sup> The second model proposes inhibition involving noncovalent binding of chloroquine to the  $\mu$ -oxo dimer.<sup>[7]</sup> The drug : dimer complex is thought to 'cap' the formation of Hmz resulting in a higher concentration of free heme in the food vacuole, which ultimately causes membrane lysis. Consequently, knowledge on the molecular and electronic structure of Hmz and model compounds is critically important in developing new antimalarial drugs.

Metalloporphyrins as mimics for biologically functional molecules have been extensively studied.<sup>[8–15]</sup> In this context, both tetraphenylporphyrin (TPP) and octaethylporphyrin (OEP) iron complexes have been the conventional models for heme systems. Crystallography and several spectroscopic techniques have been applied to investigate the molecular and electronic structure of heme compounds. Among the spectroscopic techniques, resonance Raman (RR) spectroscopy is uniquely sensitive to the stereochemical and bonding arrangements of atoms in metalloporphyrin molecules,<sup>[16]</sup> and the technique has been used to establish the correlation between heme structure and the structurally sensitive high-wavenumber Raman marker bands of  $D_{4h}$  and  $D_{2d}$  symmetry forms of Ni(OEP).<sup>[8,10–12]</sup> RR spectroscopy is also a powerful technique to investigate evidence for electronic interaction between  $\pi$  systems<sup>[17,18]</sup> including  $\pi$ – $\pi$  excitonic

\* Correspondence to: Kenneth J. Haller, School of Chemistry, Institute of Science, Suranaree University of Technology, Nakhon Ratchasima 30000, Thailand.

E-mail: ken.haller@gmail.com

\* Bayden R. Wood, Centre for Biospectroscopy and School of Chemistry, Monash University, Victoria 3800, Australia.

E-mail: bayden.wood@monash.edu

a Department of Chemistry, Faculty of Science, Maejo University, Chiang Mai 50290, Thailand

b School of Chemistry, Institute of Science, Suranaree University of Technology, Nakhon Ratchasima 30000, Thailand

c Department of Chemistry and Physics, La Trobe Institute for Molecular Science, La Trobe University, Melbourne, VIC, 3086, Australia

d Centre for Biospectroscopy and School of Chemistry, Monash University, VIC, 3800, Australia

**Abbreviations:** Fe(OEP)picrate, 2,3,7,8,12,13,17,18-Octaethylporphyrinato(picrate) iron(III);  $H_2OEP$ , 2,3,7,8,12,13,17,18-Octaethylporphyrin;  $H_2PPiX$ , 3,8,13,17-Tetramethyl-7,12-divinylporphyrin-2,18 dipropionic acid; for a generalized porphyrin;  $C_\alpha$ ,  $C_\beta$ , and  $C_m$  refer to the porphyrin core  $\alpha$ ,  $\beta$ , and meso carbon positions, respectively;  $H_2TPP$ , 5,10,15,20-Tetraphenylporphyrin

interactions, and for analyzing the effects of  $\pi$ - $\pi$  stacking.<sup>[13,19]</sup> Excitation in near-resonance with the B (Soret) band in metal porphyrins results in polarized ( $A_{1g}$ ) totally symmetric modes becoming enhanced, while excitation into the  $Q_0$  band (~575 nm) results in the enhancement of depolarized ( $B_{1g}$  and  $B_{2g}$ ) modes. Enhancement in between the  $Q_0$  and  $Q_1$  transitions results in anomalously polarized bands ( $A_{2g}$ ). Li *et al.*<sup>[20]</sup> undertook a study to examine the contribution of ethyl substituent involvement in the Ni(OEP) vibrational spectra by replacing the methylene hydrogen atoms with deuterium. The spectra showed that the strongest bands were observed in the  $1000\text{-cm}^{-1}$  region, which were assigned to modes that were predominantly ethyl in character, as revealed by their methylene-d shifts and normal coordinate analysis.<sup>[20]</sup>

Specific RR bands can be used to identify  $C_\alpha$  and  $C_\beta$  substituents. The  $\nu_2(A_{1g})$  and  $\nu_{11}(B_{1g})$  modes are sensitive to the nature of  $C_\beta$  substituents, while the  $\nu_3(A_{1g})$ ,  $\nu_{19}(A_{1g})$ , and  $\nu_{10}(B_{1g})$  modes are characteristic of  $C_\alpha$  stretching vibrations.<sup>[21]</sup> Consequently, RR spectroscopy is a powerful technique to gain structural information on the various metalloporphyrins.

In terms of coordination sphere stereochemistry,  $\mu$ -oxo iron(III) TPP and OEP porphyrins, both containing five-coordinate high-spin iron(III) coordinated to an oxygen atom from the axial ligand, are good model systems to study the molecular and electronic structure of  $\beta$ -H.<sup>[22]</sup>

We have previously reported the RR spectra of Fe(OEP)Cl, Fe(TPP)Cl, and hemin.<sup>[22]</sup> While these compounds have similar structural properties, the most similar compound in terms of the RR spectral profile is the Fe(OEP)picrate complex. As will be discussed, this can be attributed to a similar type of crystal packing of the picrate complex to  $\beta$ -H and Hmz and the number of hydrogen bonding interactions. The RR spectra of  $\beta$ -H, and of  $C_\beta$ -substituted hemes, show characteristic bands of  $C_\beta$ -substituted hemes in the ranges of 1621–1639 and 750–756  $\text{cm}^{-1}$  assigned to the  $\nu_{as}(C_\alpha C_m)$  and  $\nu(\text{pyr breathing})$  modes, respectively.<sup>[14]</sup> These bands do not appear in the spectra of  $C_m$ -substituted hemes. This work provides electronic and structural information by using Fe(OEP)picrate (Fig. 1) as a model compound for  $\beta$ -H and Hmz. Fe(OEP)picrate was chosen as a model compound for  $\beta$ -H because the solid phase, unlike that of  $[\text{Fe}(\text{OEP})]_2\text{O}$  discussed in our recent work,<sup>[22]</sup> shows the enhancement of the oxidation state marker band,  $\nu_4$ , when applying near-IR excitation laser wavelengths. The results indicate that the solid-state electronic structure of  $\beta$ -H is different to that of  $[\text{Fe}(\text{TPP})]_2\text{O}$  and  $[\text{Fe}(\text{OEP})]_2\text{O}$ , but similar to that of Fe(OEP)picrate complex. Single-crystal X-ray crystallography of the molecular and supramolecular structure of Fe(OEP)picrate and UV-Vis absorbance spectroscopy was

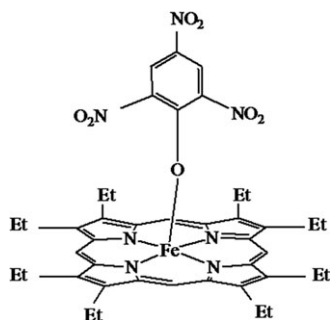


**Figure 1.** Schematic diagram of the structure of Fe(OEP)picrate.

applied to help understand the dramatic enhancement of the totally symmetric modes of  $\beta$ -H observed in the Raman profile when applying near-IR excitation wavelengths.

## Experimental

### Synthesis of Fe(OEP)picrate

Fe(OEP)Cl [0.0153 g (0.025 mmol)] (Sigma-Aldrich) was dissolved in 5 mL of dichloromethane followed by addition of 2 mL of 0.0185 M (0.037 mmol) picric acid solution. Subsequently, ~4 mL of ethanol and ~6–8 mL of dimethyl sulfoxide were added. The mixture was stirred vigorously until it was homogenous; then, 1 mL of methanol was added, and the solution allowed to stand at room temperature for 3 days. The dark blue solid product was filtered off and washed with ethanol.

It should be noted that picric acid is a known skin and eye irritant and is hazardous to ingest and inhale. It also should be noted that picric acid should never be allowed to dry out and avoid crystals forming around the cap. Picric acid becomes unstable at high temperatures and reacts strongly with oxidizing materials and can ignite in the presence of certain metals and water. Contact between picric acid and concrete floors can result in the formation of explosive salts.

### Attenuated total reflection Fourier transform infrared spectroscopy

Attenuated total reflection Fourier transform infrared spectroscopy spectra were recorded on a Bruker Equinox spectrometer. Solid Fe(OEP)picrate and Fe(OEP)Cl were placed on the window of an attenuated total reflection cell, while picric acid solution was dried onto the window. Spectra were recorded in absorption mode at  $5\text{-cm}^{-1}$  resolution with 60 interferograms co-added.

### UV-Vis absorbance spectroscopy

UV-Vis absorbance spectra were recorded by using a Cary 100 Bio UV-Vis spectrometer. Dichloromethane was used as the solvent to dissolve both Fe(OEP)picrate and Fe(OEP)Cl, while the picric acid solution was prepared by using distilled water as the solvent.

### Resonance Raman spectroscopy

Resonance Raman spectra of the products were recorded on a Renishaw system 2000 spectrometer by using 413 and 514-nm excitation lines generated by a Spectra Physics Kr<sup>+</sup>-Ar<sup>+</sup> Stabilite 2017 laser system, 633-nm excitation line from a helium-neon laser, 782-nm excitation line generated by a diode laser, and 830-nm excitation line from a diode laser. The approximate laser power at the sample is 0.039, 1.3, 1.6, 0.5, and 4.0 mW for the excitation wavelengths 413, 514, 633, 782, and 830 nm, respectively. The system was equipped with an Olympus optical microscope and a Zeiss  $\times 60$  water immersion objective to enable spectral acquisition in water to minimize thermal degradation of the solid porphyrin samples. Picric acid was dried in air before recording the RR spectrum by using the  $\times 40$  objective in the dry state. Spectra were recorded between 1800 and  $230\text{ cm}^{-1}$ . Each spectrum was accumulated as one scan with a laser exposure of 10 s. The spectral resolution is between 1 and  $2\text{ cm}^{-1}$ . The percentage of power at the sample was 10% power with 4 pixels of the charge-coupled

device binned together to improve the signal-to-noise ratio. The instrument was calibrated to the  $520.5\text{-cm}^{-1}$  Si band. No change was observed in the surfaces of the samples based on microscopic examination before and at the end of data collection. The enhancement factors were calculated relative to the largest band in the spectrum located at  $1558\text{ cm}^{-1}$ , which remained invariant for all laser wavelengths investigated except  $413\text{ nm}$ . This band was consequently chosen as the normalization band, and the enhancement factors calculated relative to its intensity. For the  $413\text{-nm}$  spectrum, the normalization band was  $1580\text{ cm}^{-1}$ , which was the most intense band in the spectrum at this excitation laser line.

## Theoretical procedures

Vibrational spectra of picric acid and the iron picrate complex were optimized by using the B3LYP/6-31G(d) and M06L/cc-pVDZ levels of density functional theory to facilitate interpretation of the experimental spectra. The B3LYP functional is widely used for its generally reliable vibrational predictions. M06 belongs to a Minnesota family functional and is designed to describe transition metal complexes. It has been used to study different biological systems.<sup>[23,24]</sup> M06L optimizations were conducted by using the conductor-like polarizable continuum model with water as the solvent. All calculations were performed with the *Gaussian09* suite of programs. Scaling for both B3LYP and M06L calculations is necessary to negate shortcomings in the prediction of stretching vibrations in particular such as basis set limitations.<sup>[25]</sup> These factors were determined individually for both levels of theory by calculating the average ratio between the experimental and predicted values.<sup>[26]</sup> Geometry optimizations preceded vibrational wavenumber value calculations, with Fe(OEP)picrate complex; the crystal structure was used as the starting structure. B3LYP geometry optimization of the free Fe(OEP)picrate monomer results in the picrate ring tilting at a greater angle to the porphyrin ring than in the more constrained crystal environment, with the  $C_{para}(\text{picrate})\text{-}C_{\alpha}(\text{heme})$  distance increased from  $4.42$  to  $5.71\text{ \AA}$ . Simulated Raman spectra were computed with Raman intensities calculated for  $830\text{-nm}$  excitation ( $\bar{\nu}_0 = 12048\text{ cm}^{-1}$ ) by using the relation:

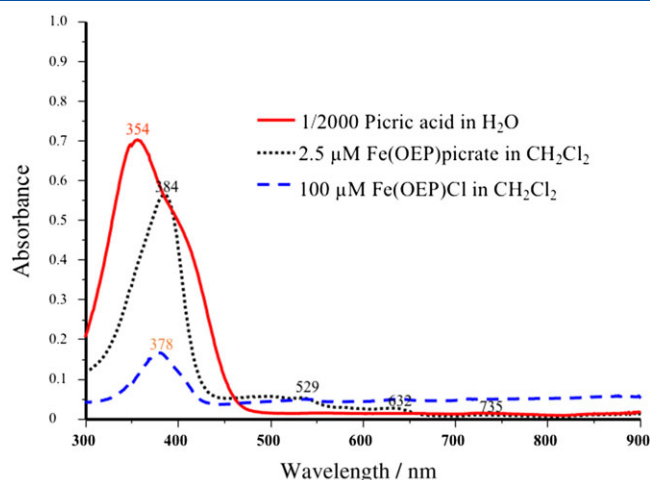
$$I_i = f(\bar{\nu}_0 - \bar{\nu}_i)^4 S_i / \bar{\nu}_i [1 - \exp(-hc\bar{\nu}_i/kT)]$$

where  $S_i$  is the calculated Raman activity for the  $i$ th mode at  $\bar{\nu}_i\text{ cm}^{-1}$ ;  $h$ ,  $c$ , and  $k$  are the fundamental constants; temperature  $T$  was assumed to be  $298\text{ K}$ , and  $f$  is a normalization factor. A Lorentzian lineshape of full-width half-maximum (FWHM) =  $10\text{ cm}^{-1}$  was applied.

## Results

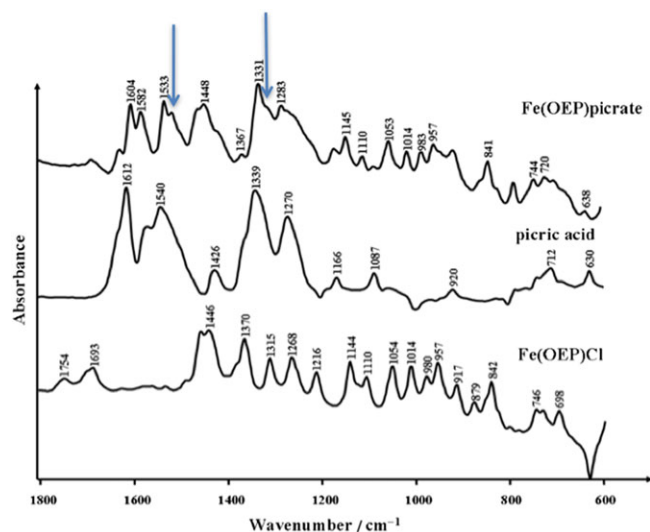
### UV-Vis spectra

Figure 2 shows the UV-Vis-near-infrared spectra of picric acid, Fe(OEP)Cl, and Fe(OEP)picrate. The Soret band for Fe(OEP)picrate is slightly red-shifted from the Fe(OEP)Cl complex from  $378$  to  $384\text{ nm}$ . The Fe(OEP)picrate complex contains the O atom from the picrate, which is a  $\pi$ -bonding ligand resulting in the Soret absorption band appearing at a longer wavelength. Picric acid, on the other hand, absorbs very strongly at  $354\text{ nm}$ . Both Fe(OEP)Cl and Fe(OEP)picrate show weak charge-transfer bands at approximately  $630\text{ nm}$  indicative of high-spin ferric hemes.<sup>[27]</sup> Fe(OEP)Cl and Fe(OEP)picrate absorb very weakly in the near-IR and show evidence of a low-lying charge-transfer transition between



**Figure 2.** UV-Vis spectra of Fe(OEP)picrate, Fe(OEP)Cl, and picric acid. [Colour figure can be viewed at [wileyonlinelibrary.com](http://wileyonlinelibrary.com)]

$700$  and  $900\text{ nm}$ . In an earlier study,<sup>[22]</sup> we presented UV-Vis spectra of Fe(TPP)Cl, Fe(OEP)Cl, [Fe(TPP)]<sub>2</sub>O, and [Fe(OEP)]<sub>2</sub>O. All spectra showed a band between  $600$  and  $690\text{ nm}$  assigned to a charge-transfer transition indicative of high-spin ferric hemes. However, no obvious electronic transition was observed in the near-IR region ( $750\text{--}900\text{ nm}$ ) where the totally symmetric modes are dramatically enhanced.<sup>[22]</sup> The UV-Vis spectra of hemin converted to  $\beta$ -H have also been reported by our group.<sup>[14]</sup> These spectra also show a charge-transfer transition indicative of high-spin ferric hemes, in this case shifting from  $612\text{ nm}$  in hemin to  $649\text{ nm}$  in  $\beta$ -H. Upon conversion to  $\beta$ -H, we noted a small broad low-lying transition centered at  $867\text{ nm}$  that we assigned to a z-polarized charge-transfer transition  $d_{xy} \rightarrow e_g(\pi^*)$ . The extraordinary band enhancement observed when exciting with near-infrared excitation wavelengths in  $\beta$ -H when compared with hemin was explained in terms of an aggregated enhanced Raman scattering hypothesis based on the intermolecular excitonic interactions between porphyrinic units that occurs upon excitation into this broad low-lying electronic transition centered at  $867\text{ nm}$ .<sup>[28]</sup> Ali and Openeer<sup>[29]</sup> recently performed high-level time-dependent density



**Figure 3.** Attenuated total reflection Fourier transform infrared spectra of Fe(OEP)picrate, picric acid, and Fe(OEP)Cl. [Colour figure can be viewed at [wileyonlinelibrary.com](http://wileyonlinelibrary.com)]

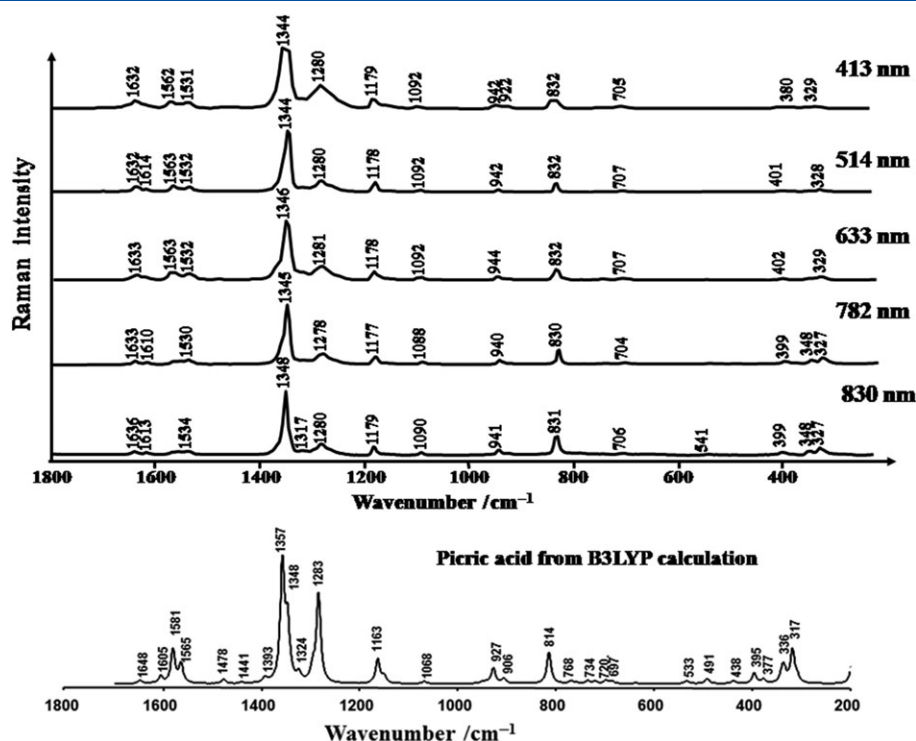


**Figure 4.** Experimental Raman spectra of deep yellow solid-state picric acid along with a normal Raman simulation from the B3LYP/6-31G(d) calculation.

**Table 1.** Observed peak positions ( $\text{cm}^{-1}$ ) compared with predicted band positions, strengths, and local coordinate assignments for picric acid

Experimental					Calculated B3LYP/6-31G*				
Raman					IR	Scaled $\times 0.970$	IR int	Raman activity	Mode description
413 nm	514 nm	633 nm	782 nm	830 nm	$\text{cm}^{-1}$	$\text{cm}^{-1}$	$\text{km mol}^{-1}$	$\text{\AA}^4 \text{amu}^{-1}$	
1632	1632	1633	1633	1636	—	1648	278	7.5	Ring CC str
—	1614	—	1610	1613	1612	1622	298	0.7	$\text{NO}_2$ antisym ( <i>para</i> )
—	—	—	—	—	—	1606	110	15	$\text{NO}_2$ antisym ( <i>ortho</i> ) + OH bend
1562	1563	1563	—	—	—	1581	16	73	CC ring str + OH bend
1531	1532	1532	1530	1534	1540	1565	41	42	$\text{NO}_2$ antisym + CC ring str
—	—	—	—	—	—	1478	87	9.3	CO str (and CH in plane bend)
—	—	—	—	—	1426	1441	220	3.1	OH bend
—	—	—	—	—	—	1393	24	8.7	Ring str (+ OH bend)
1344	1344	1346	1345	1348	—	1358	149	201	$\text{NO}_2$ symstr (sym comb of <i>para</i> + non-H-bonded)
—	—	—	—	—	1339	1347	349	98	$\text{NO}_2$ symstr (antisym comb of <i>para</i> + non-H-bonded)
—	—	—	—	—	—	1324	196	14	Ring CC str
—	—	—	—	—	—	1296	102	23	Ring CC, OH, and CH in plane bends
1280	1280	1281	1278	1280	1270	1284	158	140	$\text{NO}_2$ symstr (H-bonded <i>ortho</i> ) + OH and CH bends
1179	1178	1178	1177	1179	—	1163	17	33	Sym CN str (all three)
—	—	—	—	—	—	1151	44	9.7	CH and OH in plane bend
1092	1092	1092	1088	1090	1087	1069	88	3.0	$\text{CH}_2$ in plane bend
—	—	—	—	—	—	949	0.8	2.1	$\text{CH}_2$ out of plane (antisym)
—	—	—	—	—	—	941	18	1.1	$\text{CH}_2$ out of plane (sym)
942	942	944	940	941	—	928	32	16	<i>para</i> -CN str (+ other 2)
—	—	—	—	—	—	906	65	5.0	<i>ortho</i> -CN antisymstr
832	832	832	830	831	—	815	0.3	23	In plane ring def + $\delta$ (ONO) sym
—	—	—	—	—	—	812	2.3	3.8	$\delta$ (ONO) <i>para</i> (+ in plane ring def)
—	—	—	—	—	—	769	44	2.1	HO out of plane def

**Table 2.** Observed Raman band ( $\text{cm}^{-1}$ ), assignments, symmetry terms, and local coordinates and relative enhancement factors for Fe(OEP)picrate at 413, 514, 633, 782, and 830-nm excitation

Fe(OEP)picrate		M06L/cc-pVDZ					B3LYP/6-31G*					Assignment <sup>a</sup> Symmetry	
		Scaled 0.987	Ram act $\text{\AA}^4 \text{amu}^{-1}$	Local coordinates	Scaled 0.970	Ram act $\text{\AA}^4 \text{amu}^{-1}$	Local coordinates	Scaled 0.970	Ram act $\text{\AA}^4 \text{amu}^{-1}$	Local coordinates			
413	1630(10)	1637	512	Ring CC str (pic)	1630	201	$\nu(\text{C}_\alpha\text{C}_m)_{\text{asym}}$	—	—	$\nu_{10}$	—	—	
—	—	1623	125	$\nu(\text{C}_\beta\text{C}_\beta)$	—	—	—	—	—	—	—	—	
—	—	1618	133	$\nu(\text{NO}_2)_{\text{asym}}$ ring CC str (pic)	1616	100	$\nu(\text{NO}_2)_{\text{asym}}$ ring CC str (pic)	—	—	—	—	—	
—	—	1615	579	$\nu(\text{C}_\alpha\text{C}_m)_{\text{asym}}$	—	—	—	—	—	—	—	—	
—	—	1613	11295	$\nu(\text{C}_\beta\text{C}_\beta)$	—	—	—	—	—	—	—	—	
1580(10)	—	1594	767	$\nu(\text{NO}_2)_{\text{asym}}$	1580	1027	$\nu(\text{C}_\beta\text{C}_\beta)$	—	—	$\nu_2$	—	—	
—	1570(7)	1590	10876	$\nu(\text{C}_\beta\text{C}_\beta)$	—	—	$\nu(\text{C}_\alpha\text{C}_m)_{\text{asym}}$	—	—	$\nu_{19}$	—	—	
—	1558(6)	1557	140	$\nu(\text{C}_\alpha\text{C}_m)_{\text{asym}}$	1555	1475	$\nu(\text{C}_\beta\text{C}_\beta)$	—	—	$\nu_{11}$	—	—	
1495(4)	1492(1)	1492	345	$\nu(\text{C}=\text{O})$ (pic)	—	—	$\delta(\text{C}_\alpha\text{C}_m)_{\text{sym}}$	—	—	$\nu_3$	—	—	
—	—	1466	159	$\delta(\text{C}_\alpha\text{C}_m)_{\text{sym}}$	1480	73	$\delta(\text{C}_\alpha\text{C}_m)_{\text{sym}}$	—	—	$\nu_{28}$	—	—	
—	1456(1)	1466	159	$\delta(\text{C}_\alpha\text{C}_m)_{\text{sym}}$	—	—	$\nu(\text{pyr}$ quarter-ring)	—	—	$\nu_{29}$	—	—	
—	1404(4)	1403	302	$\nu(\text{pyr}$ quarter-ring)	—	—	$\nu(\text{pyr}$ quarter-ring)	—	—	$\nu_{20}$	—	—	
—	—	—	—	$\nu(\text{pyr}$ quarter-ring)	—	—	$\nu(\text{pyr}$ half-ring) <sub>sym</sub>	—	—	$\nu_4$	—	—	
1377(8)	1376(5)	1386	2277	$\nu(\text{pyr}$ half-ring) <sub>sym</sub>	1383	240	$\nu(\text{pyr}$ half-ring) <sub>sym</sub>	—	—	—	—	—	
1333(1)	1334(2)	1336	4299	$\nu(\text{ethyl})_{\text{sym}} + \nu(\text{NO}_2)_{\text{sym}}$	1343	714	$\nu(\text{ethyl})_{\text{sym}} + \nu(\text{NO}_2)_{\text{sym}}$	—	—	—	—	—	
1315(1)	1308(3)	1296	133	$\delta(\text{C}_m\text{H})$ Ethyl	1330	118	$\delta(\text{C}_m\text{H})$ Ethyl	—	—	$\nu_{21}$	—	—	
—	—	1271	189	—	1279	82	—	—	—	—	—	—	
1261(1)	—	b	—	$\delta(\text{C}_\beta\text{C}_1)_{\text{sym}}$	1264	33	$\delta(\text{C}_m\text{H})_{\text{asym}}$ Ethyl	—	—	$\nu_5 + \nu_9$	—	—	
1213(1)	1212(2)	1234	1028	$\delta(\text{C}_m\text{H})$	1208	254	$\delta(\text{C}_m\text{H})$	—	—	$\nu_{13}$	—	—	
—	—	1168	411	$\nu(\text{CN}$ of picrate) <sub>sym</sub>	1161	68	$\nu(\text{CN}$ of picrate) <sub>sym</sub>	—	—	—	—	—	
—	1155(2)	—	—	$\nu(\text{pyr}$ half-ring) <sub>asym</sub>	—	—	$\nu(\text{pyr}$ half-ring) <sub>asym</sub>	—	—	$\nu_{30}$	—	—	
1131(1)	—	b	—	$\nu(\text{C}_\alpha\text{C}_\beta)_{\text{sym}} + \nu(\text{Fe-N})$	—	—	$\nu(\text{C}_\alpha\text{C}_\beta)_{\text{sym}} + \nu(\text{Fe-N})^a$	—	—	$\nu_6 + \nu_8$	—	—	
—	1135(3)	—	—	$\nu(\text{pyr}$ half-ring) <sub>asym</sub>	—	—	$\nu(\text{pyr}$ half-ring) <sub>asym</sub>	—	—	$\nu_{22}$	—	—	
—	1125(1)	1139	278	$\nu(\text{pyr}$ half-ring) <sub>asym</sub>	1124	42	$\nu(\text{pyr}$ half-ring) <sub>asym</sub>	—	—	$\nu_{23}$	—	—	
—	—	1067	210	$\nu(\text{C}_\beta\text{C}_1)_{\text{asym}}$	1057	27	$\nu(\text{C}_\beta\text{C}_1)_{\text{asym}}$	—	—	$\nu_5$	—	—	
1024(1)	1025(2)	1067	—	$\nu(\text{C}_\beta\text{C}_1)_{\text{sym}}$	1018	14	$\delta(\text{C}_m\text{H})$	—	—	$\nu_{32} + \nu_{35}$	—	—	
—	962(1)	b	—	$\delta(\text{porph}$ def) + $\delta(\text{pyr}$ def)	947	36	$\delta(\text{porph}$ def) + $\delta(\text{pyr}$ def)	—	—	—	—	—	
—	—	—	—	$\delta(\text{porph}$ def) + $\delta(\text{pyr}$ def)	—	—	$\nu(\text{C-C})_{\text{sym}}$ Ethyl	—	—	—	—	—	
869(1)	—	—	—	Ethyl	—	—	Ethyl	—	—	—	—	—	
—	—	—	—	$\delta(\text{ethyl})_{\text{sym}}$ (porph)	—	—	$\delta(\text{ethyl})_{\text{sym}}$ (porph)	—	—	—	—	—	
802(1)	—	—	—	$\nu(\text{ethyl}$ deform)	—	—	$\nu(\text{ethyl}$ deform)	—	—	$\nu_6$	—	—	
—	786(1)	—	—	$\delta(\text{ethyl}$ deform) <sub>asym</sub>	—	—	$\delta(\text{ethyl}$ deform) <sub>asym</sub>	—	—	$\nu_{32}$	—	—	
—	—	—	—	$\nu(\text{pyr}$ breathing + Ethyl deform)	—	—	$\nu(\text{pyr}$ breathing + Ethyl deform)	—	—	$\nu_{47}$	—	—	
—	—	—	—	$\nu(\text{pyr}$ breathing + Ethyl deform)	—	—	$\nu(\text{pyr}$ breathing + Ethyl deform)	—	—	—	—	—	
755(1)	752(1)	—	—	$\nu(\text{pyr}$ breathing + Ethyl deform)	—	—	$\nu(\text{pyr}$ breathing + Ethyl deform)	—	—	$\nu_{15}$	—	—	
—	—	—	—	$\nu(\text{pyr}$ breathing + Ethyl deform)	—	—	$\nu(\text{pyr}$ breathing + Ethyl deform)	—	—	—	—	—	
672(1)	672(1)	675	235	Ethyl deform)	660	12	$\delta(\text{porph}$ def) <sub>sym</sub>	—	—	$\nu_7$	—	—	
—	—	—	—	Ethyl deform)	—	—	—	—	—	—	—	—	

(Continues)

Table 2. (Continued)

Fe(OEP)picrate	M06L/cc-pVDZ				B3LYP/6-31G*				Assignment <sup>a</sup>	Symmetry				
	514	633	782	830	Scaled 0.987	Ram act $\text{\AA}^4 \text{amu}^{-1}$	Local coordinates	Scaled 0.970			Ram act $\text{\AA}^4 \text{amu}^{-1}$	Local coordinates		
413	—	—	—	—	507(1)	—	—	—	—	—	—	—	—	—
—	—	—	—	—	474(1)	—	—	—	—	—	—	—	—	—
461(1)	—	464(1)	—	464(1)	—	463	—	—	—	—	—	—	—	—
—	—	—	—	—	456(1)	—	—	—	—	—	—	—	—	—
398(1)	402(1)	400(1)	400(1)	400(1)	400(2)	394	—	—	—	—	—	—	—	—
—	—	—	—	—	353(2)	—	—	—	—	—	—	—	—	—
344(1)	—	345(1)	—	341(3)	—	—	—	—	—	—	—	—	—	—
—	332(1)	—	—	329(2)	—	—	—	—	—	—	—	—	—	—
—	—	268(1)	266(1)	264(2)	—	—	—	—	—	—	—	—	—	—

<sup>a</sup>Mode numbering is based on that originally proposed by M. Abe, T. Kitagawa, and Y. Kyogoku, Resonance Raman spectra of octaethylporphyrinato-Ni(II) and meso-deuterated and 15 N substituted derivatives. A normal coordinate analysis, *J. Chem. Phys.* 69, 4526–4534, 1978. Local coordinates were assigned based on comparison of the observed bands with those from frequency calculations at the B3LYP/6-31G(d) and M06L/cc-pVDZ levels of theory.

<sup>b</sup>Bands that were not observed in the experimental spectra.

functional theory (DFT) calculations to simulate the UV-Vis absorption spectrum of Hmz. The theoretical spectra matched very well with the available experimental spectra. The lowest energy electronic transition at 880 nm was found to be completely due to spin-polarized electronic transitions of one spin type only. The authors also used calculations to predict a high-spin  $S = 5/2$  on each of the Fe centers, in addition to a weak intramolecular antiferromagnetic exchange coupling between the two Fe centers, which results in a singlet state for the minimum of the potential energy surface. It appears that compounds including  $\beta$ -H and Fe (OEP)picrate, which exhibit enhanced totally symmetric modes when exciting with near-IR, have broad low-energy electronic transitions in the 700 to 900-nm region of the electromagnetic spectrum.

### Infrared spectra

Attenuated total reflection Fourier transform infrared spectra are shown in Fig. 3. In this section the results discussed are the B3LYP calculations. The spectrum of the complex contains features derived from both the picric acid and the OEP components, but is not a simple linear addition. According to the DFT calculations, the normal coordinate composition of the  $\text{NO}_2$  and CC ring stretch modes changes in the complex, in part due to changes in the bonding and possibly due to the sterically induced rotation of the *ortho*- $\text{NO}_2$  functional groups. This leads to shifts in the band positions and intensities between picric acid and the complex. For example, the band at  $1612 \text{ cm}^{-1}$  in picric acid, tentatively assigned to two close lying  $\nu_{\text{as}}(\text{NO}_2)$  modes, is mixed with the CC ring stretching from the porphyrin. Bands at  $1339$  and  $1270 \text{ cm}^{-1}$  are assigned to the nitro group symmetric stretches,  $\nu_{\text{s}}(\text{NO}_2)$ , in picric acid.<sup>[18]</sup> The  $\nu_{\text{as}}(\text{NO}_2)$  modes in the Fe (OEP)picrate spectrum are split into two bands at  $1604$  and  $1582 \text{ cm}^{-1}$  due to the different molecular environments of the *ortho* and *para*-substituted  $\text{NO}_2$  groups, and a further pair of bands appears at  $1533$  and  $1520 \text{ cm}^{-1}$ . The corresponding *ortho*- $\nu_{\text{s}}(\text{NO}_2)$  split modes appear at  $1331 \text{ cm}^{-1}$  along with a shoulder feature at  $\sim 1320 \text{ cm}^{-1}$ . A number of bands can be directly assigned to the OEP that appear both in Fe(OEP)picrate and Fe(OEP)Cl. These include bands at  $1470$ ,  $1446$ ,  $1370$ ,  $1315$ ,  $1110$ ,  $1054$ ,  $1014$ ,  $980$ ,  $957$ ,  $879$ , and  $842 \text{ cm}^{-1}$ , which are absent in the RR spectra. Fonda *et al.*<sup>[30]</sup> reported that the IR spectrum of Cu(octaethylchlorin) exhibited seven modes  $1464$ ,  $1452$ ,  $1375$ ,  $1064$ ,  $1058$ ,  $1015$ , and  $956 \text{ cm}^{-1}$ , which are in very similar positions to the bands observed in Fe(OEP)picrate. These bands were insensitive to metal substitution, methine deuteration, and changes in peripheral substituents and hence were assigned to ethyl group vibrations.<sup>[30]</sup> They also noted that these modes did not appear in the RR spectra, except for the  $1464 \text{ cm}^{-1}$  band that was present in nearly all of the RR spectra of the chlorin complexes that they examined.<sup>[30]</sup> Kincaid *et al.*<sup>[31]</sup> reported high-resolution infrared spectra of divalent metal (Mn, Fe, Co, Ni, Cu, Zn) complexes of octaethylporphine obtained at  $-15 \text{ K}$  in argon matrices or as thin films. They observed bands at  $1473$  and  $1456 \text{ cm}^{-1}$  in Ni(OEP), similar in position to bands observed at  $1470$  and  $1446 \text{ cm}^{-1}$  in the Fe(OEP)picrate complex in this work, that they assigned to ethyl group vibrations. They found that the  $\delta_{\text{sym}}(\text{CH}_3)$  moiety of the ethyl group was observed as a medium-intensity band within the  $1375$  to  $1385 \text{ cm}^{-1}$  region, whereas we observe a similar band at  $1370 \text{ cm}^{-1}$ , which is also assigned to this mode in the Fe(OEP)picrate complex. Kincaid *et al.*<sup>[21]</sup> assigned bands at  $1119$ ,  $1069$ ,  $1061$ , and  $1021 \text{ cm}^{-1}$  to ethyl group vibrations in Ni(OEP), which correlate to bands at  $1110$ ,  $1054$ ,

and  $1014\text{ cm}^{-1}$  in the Fe(OEP)picrate complex. Kincaid *et al.*<sup>[31]</sup> also assigned a band at  $959\text{ cm}^{-1}$  to an ethyl group vibration, and we observe a similar intensity band at  $954\text{ cm}^{-1}$  corresponding to this assignment.

## Raman spectra

Experimental Raman spectra of deep yellow solid-state picric acid are compared with a normal Raman calculation from B3LYP/6-31G(d) results in Fig. 4. Observed and predicted band positions are listed in Tables 1 and 2, respectively. DFT calculations have previously been performed on  $\beta$ -H by using BP86/SDD level of theory.<sup>[32,33]</sup> We have applied a higher level of theory to examine the Fe(OEP)picrate complex. The bands at approximately  $1610$ ,  $1345$ , and  $832\text{ cm}^{-1}$  are assigned to the  $\nu_{\text{as}}(\text{NO}_2)$ ,  $\nu_{\text{s}}(\text{NO}_2)$ , and the in-plane (scissoring) deformation  $\delta(\text{NO}_2)$ , respectively, of the aromatic  $\text{NO}_2$  groups of picric acid. These bands appear at  $1604$ ,  $1348$ , and  $814\text{ cm}^{-1}$  in the calculated spectrum. Figure 5 compares experimental RR spectra of Fe(OEP)picrate with the B3LYP-predicted spectrum computed. Perhaps rather surprisingly, this level of theory appeared to reproduce the observed band profile better than M06L/cc-pVDZ. Table 2 compares the band positions observed in the spectrum of the complex with corresponding values computed at both B3LYP/6-31G(d) and M06L/cc-pVDZ levels of theory. The Fe(OEP)picrate complex shows Raman bands at  $1607$  and  $1333\text{--}1339\text{ cm}^{-1}$  in the region of  $\nu_{\text{as}}(\text{NO}_2)$  and  $\nu_{\text{s}}(\text{NO}_2)$ ,<sup>[34]</sup> observed when using near-IR excitation wavelengths that are shifted compared with the respective positions for picric acid ( $1610\text{--}1613$  and  $1345\text{--}1348\text{ cm}^{-1}$ ), indicating that the N–O

bonding is weaker. The agreement of observed and predicted spectral shifts between bands in picric acid and the picrate complex confirms the assignments.

The B3LYP predictions of the Raman bands seen in the picrate complex are assigned to porphyrin modes. The spin-state marker band,  $\nu_{10}$  ( $\text{C}_\alpha\text{--C}_m$  stretch), at  $\sim 1630\text{ cm}^{-1}$  is in agreement with the empirical correlation between the position of  $\nu_{10}$  for five-coordinate high-spin Fe(OEP) derivatives<sup>[35]</sup> and is also a normal value for an Fe(III) heme with a strong  $\pi$  acceptor axial ligand such as picrate.<sup>[35]</sup>  $\nu_4$ , which is a pyrrole half-ring stretching mode, is observed at  $1375\text{--}1378\text{ cm}^{-1}$ , indicating iron(III).<sup>[35]</sup> The  $\nu_4$  band is shifted to  $1372\text{ cm}^{-1}$  in Fe(OEP)Cl due to the effect of retention of planar pyrrole units on the geometry of the 16-membered ring and the resulting induced vibrational wavenumber value shifts.<sup>[10]</sup> Binding of the picrate O atom as a  $\pi$  acceptor axial ligand to Fe competes with Fe  $d_\pi \rightarrow$  porphyrin  $\pi^*$  backbonding, thereby slightly increasing the wavenumber value of the  $\nu_4$  band,<sup>[36–38]</sup> and changes the symmetry of the heme complex. It should be noted that not only is the  $\nu_4$  band sensitive to the back donation into porphyrin  $\pi^*$  and  $\pi$ -acid ligand orbitals of iron  $\pi$  electrons,<sup>[37]</sup> but it is also sensitive to the oxidation and spin state.<sup>[36]</sup> The predicted B3LYP spectrum shows  $\nu_4$  at  $1366\text{ cm}^{-1}$ , which is in fairly good agreement with the experimental spectrum. The band at  $1480\text{ cm}^{-1}$  dominates the calculated spectrum but appears very weak and shifted to  $\sim 1495\text{ cm}^{-1}$  in the experimental spectrum. This mode is a complex mode involving a number of ethyl  $\text{CH}_2$  deformation modes. The reason for its diminished intensity in the experimental spectrum is that the ethyl deformation modes are not subject to resonance effects that enhance the heme modes. Alternatively, the intensity calculation fails as there are so many degenerate

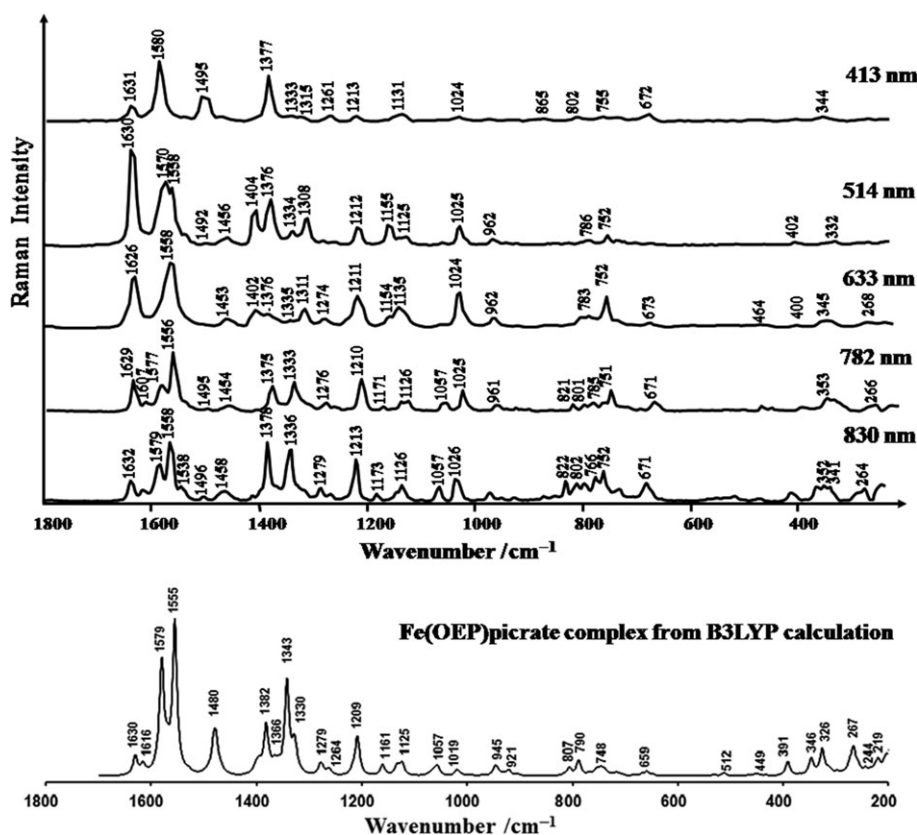


**Figure 5.** Resonance Raman spectra of Fe(OEP)picrate along with a normal Raman simulation from the B3LYP/6-31G(d) calculation.

modes. The M062X spectrum is in good agreement with the assignment of experimental vibrational modes based on the B3LYP spectrum (for more detail, refer to Table 2).

Early studies suggested that saturated alkyl substituents are not generally thought to couple electronically to aromatic chromophores, although the influence of inductive and hyperconjugative effects is readily seen in shifts of the electronic transition energies.<sup>[39]</sup> Li *et al.*,<sup>[20]</sup> on the other hand, reported that the orientation of the ethyl substituents places the  $\sigma$  orbital in the proper orientation to interact with the  $\pi^*$  orbital. Consequently, the ethyl coordinates, especially  $C_1C_2$  stretching, can induce significant excited-state origin shifts and Q/B vibronic coupling.<sup>[20]</sup>

The mean spectra of Fe(OEP)picrate and  $\beta$ -H synthesized by the acidification of hematin with glacial acetic acid<sup>[22]</sup> show similar

patterns of relative enhancement factors when comparing the same applied Raman excitation wavelength especially when applying near-IR excitation (Fig. S1). Figure 6 displays the relative enhancement factors of Fe(OEP)picrate and  $\beta$ -H for the totally symmetric  $A_{1g}$  mode,  $\nu_4$ , assigned to  $1370\text{--}1375\text{ cm}^{-1}$  [ $\nu(\text{pyr-half-ring})_{\text{sym}}$ ] and the nontotally symmetric  $B_{1g}$  mode,  $\nu_{15}$ , assigned to  $750\text{ cm}^{-1}$  [ $\nu(\text{pyr-breathing})$ ]. For both modes, the enhancement factors are comparable between the two complexes. The  $\nu_4$  band is enhanced when exciting with 413-nm wavelength laser source but is weaker when excited with 514 nm and is much weaker when applying 633-nm excitation, while it is stronger when using 782-nm excitation wavelength and completely dominates the Raman spectrum when the 830-nm excitation wavelength is applied. Moreover, Fe(OEP)picrate and  $\beta$ -H are also comparable in the appearance of ring and pyrrole breathing modes such as the bands at  $970\text{--}976\text{ cm}^{-1}$ ,  $\delta_{\text{as}}(\text{pyr deformation})$ ,  $670\text{--}678\text{ cm}^{-1}$ ,  $\delta_{\text{s}}(\text{pyr deformation})$ ,  $821\text{--}822\text{ cm}^{-1}$ ,  $\gamma(\text{C}_m\text{H})$ , and  $801\text{--}802$  and  $751\text{--}752\text{ cm}^{-1}$ ,  $\nu(\text{pyr breathing})$ . Thus, the enhancement of Fe(OEP)picrate modes throughout the spectrum is very similar to that of  $\beta$ -H for all modes related to the conformation of the porphyrin plane at all excitation wavelengths investigated.

## Discussion

Fe(OEP)picrate serves as a good model compound for  $\beta$ -H and Hmz because it has similar bands in terms of intensity and position to these compounds, especially when exciting with 830 nm. Fe(OEP)picrate shows bands at  $1627$  and  $751\text{ cm}^{-1}$  that are characteristic of *beta*-substituted hemes, which are observed in OEP derivatives. Neither of these bands appear in the spectra of Fe(TPP)Cl, [Fe(TPP)]<sub>2</sub>O, and dimethyl ester of protoheme. Another reason for choosing Fe(OEP)picrate as a model compound for  $\beta$ -H and Hmz

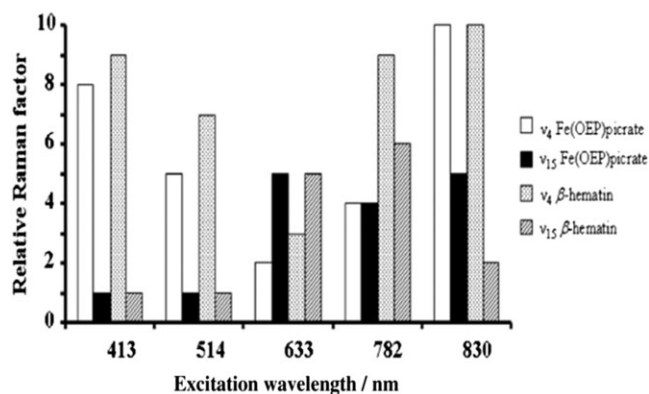


**Figure 6.** Enhancement factors of  $\nu_4$  and  $\nu_{15}$  following vector normalization over the  $1800\text{--}2000\text{ cm}^{-1}$  for Fe(OEP)picrate and  $\beta$ -hematin.

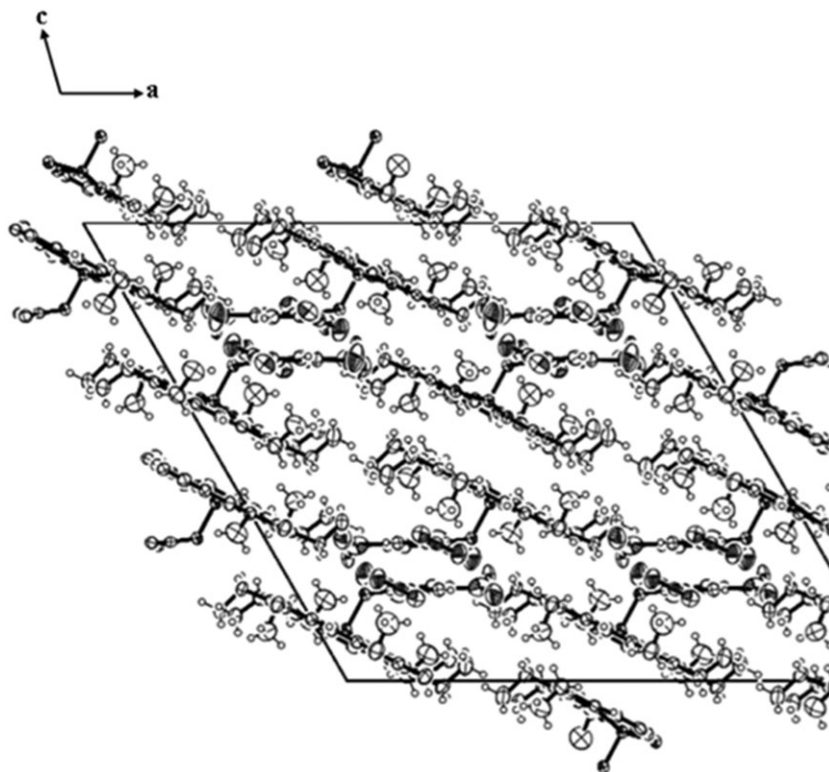


**Figure 7.** The crystal packing of Fe(OEP)picrate.

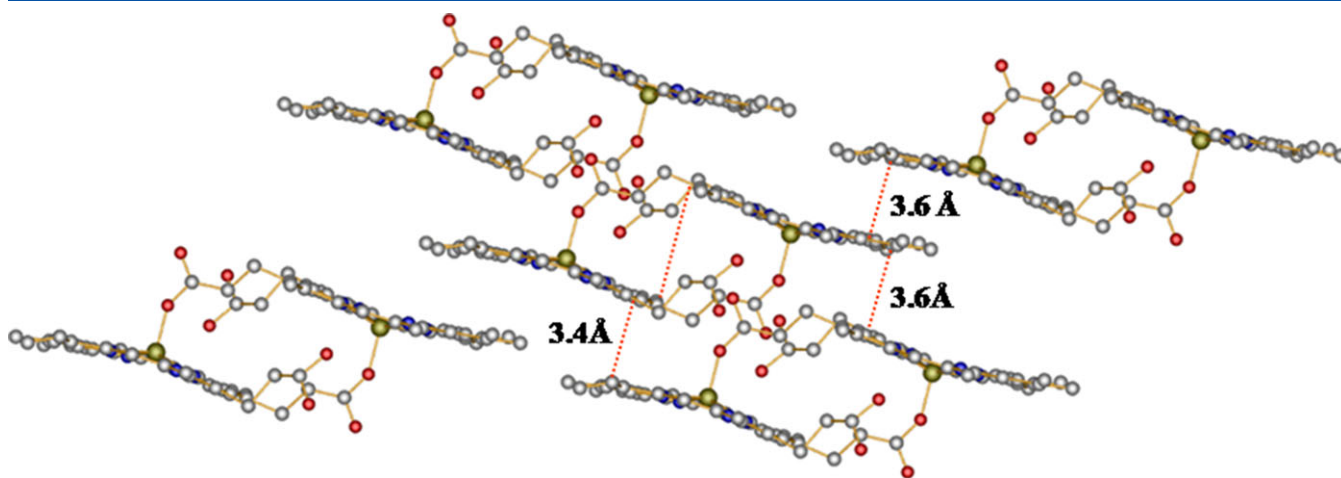


**Figure 8.** Closest porphyrin plane to porphyrin plane contact distance for  $\beta$ -hematin molecules in the crystal structure. Projection diagram drawn by DIAMOND program using XETXUP from the CSD. [Colour figure can be viewed at [wileyonlinelibrary.com](http://wileyonlinelibrary.com)]

is that it shows the enhancement of the oxidation state marker band,  $\nu_4$ , when applying near-IR excitation laser wavelengths. Neither  $[\text{Fe}(\text{OEP})_2\text{O}]$ ,  $\text{Fe}(\text{OEP})\text{Cl}$ , nor hemin show this dramatic enhancement. Furthermore,  $\text{Fe}(\text{OEP})\text{Cl}$  has chloride as the axial ligand, which is different from  $\text{Fe}(\text{OEP})\text{picrate}$  that has oxygen as axial ligand same as  $\beta$ -H.

#### Implications for intermolecular interaction of $\text{Fe}(\text{OEP})\text{picrate}$ in $\beta$ -hematin

$\text{Fe}(\text{OEP})\text{picrate}$  shows a similar Raman enhancement profile to that of  $\beta$ -H in both stretching and bending modes of pyrrole breathing, indicating that they are similar in chromophoric and electronic structure. Moreover,  $\text{Fe}(\text{OEP})\text{picrate}$  could resemble  $\beta$ -H in the conformation of the porphyrin core.

To predict the intermolecular interaction and crystal packing of  $\beta$ -H, we used the correlation of the enhancement of the  $\nu_4$  band of  $\text{Fe}(\text{OEP})\text{picrate}$  and  $\beta$ -H when applying near-IR excitation wavelengths including 782 and 830 nm. It was hypothesized that the enhancement of the totally symmetric mode at near-IR excitation wavelengths could in part be attributed to supramolecular interaction. This implies that the study of crystal structures of malaria pigment models may be a very fruitful source of information on intermolecular interaction of  $\beta$ -H. Thus, it is hypothesized that the porphyrin core planes of  $\beta$ -H and  $\text{Fe}(\text{OEP})\text{picrate}$  are very similar in terms of symmetry and intramolecular and intermolecular hydrogen bond contacts.

Analysis of the crystal packing of  $\text{Fe}(\text{OEP})\text{picrate}$  in Fig. 7 shows extensive  $\pi$ - $\pi$  stacking between adjacent porphyrin cores as well as through the components of the axial ligand. However, there is considerably less  $\pi$ - $\pi$  stacking in  $\beta$ -H due to the propionate linkage, but additional intermolecular interactions do occur via the strong propionic acid hydrogen bond linkage.<sup>[22]</sup> The closest intermolecular distance from carbon to carbon atoms in the heme ring between dimeric  $\beta$ -H is 3.435(2) Å (Fig. 8), which is almost the same as the closest distance observed in the  $\text{Fe}(\text{OEP})\text{picrate}$ , i.e. 3.443(3) Å (Fig. 7), further emphasizing the similarity of these structures in terms of intermolecular interactions. The electronic spectra are also similar with both showing a weak broad near-IR transition between 800 and 900 nm and a charge-transfer band centered around 630 nm.

The enhancement of the vibrational mode  $\nu_4$  in  $\beta$ -H when using near-IR laser excitation indicates that  $\beta$ -H contains more supramolecular interactions compared with other heme dimers and monomers based on examination of the number of intermolecular bonds as deduced by the analysis of structures generated by using ORTEP-III.<sup>[22]</sup> This is consistent with  $\beta$ -H having strong hydrogen bonds to the propionate linkage. In this case, the relative intensity of  $\nu_4$  may be an indicator of both the strength of  $\pi$ - $\pi$  and supramolecular interactions.

#### Conclusion

$\text{Fe}(\text{OEP})\text{picrate}$  was synthesized by the reaction of  $\text{Fe}(\text{OEP})\text{Cl}$  and picric acid. The molecular structure information provided by RR spectroscopy correlates well with that from single-crystal X-ray crystallographic analysis<sup>[40]</sup>; both techniques verify  $\text{Fe}(\text{OEP})\text{picrate}$  to be a five-coordinate high-spin iron(III) complex.  $\text{Fe}(\text{OEP})\text{picrate}$  is a good model to understand the stereochemistry of  $\beta$ -H based on the similar enhancement of the totally symmetric mode  $\nu_4$  and nontotally symmetric mode  $\nu_{15}$  which is assigned to  $\nu(\text{pyrrole breathing})$  at every excitation wavelength. Moreover, the enhancement of pyrrole-related modes in the 670 to 850- $\text{cm}^{-1}$  range of  $\text{Fe}(\text{OEP})\text{picrate}$  when using near-IR excitation further demonstrates the structural similarity to  $\beta$ -H. The enhancement of  $\nu_4$  is greater for  $\beta$ -H than  $\text{Fe}(\text{OEP})\text{picrate}$  because  $\beta$ -H contains a closer intermolecular porphyrin ring and extensive hydrogen bonding in comparison with  $\text{Fe}(\text{OEP})\text{picrate}$ . This work indicates that  $\beta$ -H contains more supramolecular interactions compared with  $\text{Fe}(\text{OEP})\text{picrate}$  and supports the notion that  $\beta$ -H is linked by the hydrogen-bonded propionate.

#### Acknowledgements

R. Puntharod acknowledges financial support from the Office of the Commission of Higher Education, Thailand. This work is supported by an Australian Research Council (ARC) Discovery Grant DP140102504. BRW is supported by an ARC Future Fellowship grant FT120100926. The authors gratefully acknowledge a generous allocation of computer resources through the Monash eResearch Centre and the National Computational Infrastructure in Canberra.

## References

- [1] A. Gulland, *BMJ* **2012**, 345.
- [2] P. A. Holding, R. W. Snow, *Am. J. Trop. Med. Hyg.* **2001**, *64*, 68.
- [3] A. Björkman, *Int. J. Parasitol.* **2002**, *32*, 1637.
- [4] E. Tjitra, N. M. Anstey, P. Sugiarto, N. Warikar, E. Kenangalem, M. Karyana, D. A. Lampah, R. N. Price, *PLoS Med.* **2008**, *5*, e128.
- [5] A. F. G. Slater, W. J. Swiggard, B. R. Orton, W. D. Flitter, D. Goldberg, A. Cerami, G. B. Henderson, *Proc. Natl. Acad. Sci. U. S. A.* **1991**, *88*, 352.
- [6] S. Pagola, P. W. Stephens, D. S. Bohlé, A. D. Kosar, S. K. Madsen, *Nature* **2000**, *404*, 307.
- [7] S. Moreau, B. Perly, J. Biguet, *Biochimie* **1982**, *64*, 1015.
- [8] P. M. Callahan, G. T. Babcock, *Biochemistry* **1981**, *20*, 952.
- [9] T. G. Spiro, T. C. Streckas, *J. Am. Chem. Soc.* **1974**, *96*, 338.
- [10] L. D. Spaulding, C. C. Chang, N.-T. Yu, R. H. Felton, *J. Phys. Chem. Soc.* **1975**, *97*, 2517.
- [11] D. M. Scholler, M. Y. Wang, B. M. Hoffman, *J. Biol. Chem.* **1979**, *254*, 4072.
- [12] T. G. Spiro, J. D. Stong, P. Stein, *J. Am. Chem. Soc.* **1979**, *101*, 2648.
- [13] L. D. Sparks, W. R. Scheidt, J. A. Shelnut, *Inorg. Chem.* **1992**, *31*, 2191.
- [14] B. R. Wood, S. Langford, B. M. Cooke, J. Lim, F. K. Glenister, M. Duriska, J. Unthank, D. McNaughton, *J. Am. Chem. Soc.* **2004**, *126*, 9233.
- [15] F. Paulat, V. K. K. Praneeth, C. Näther, N. Lehnert, *Inorg. Chem.* **2006**, *45*, 2835.
- [16] T. G. Spiro, *Biological Applications of Raman Spectroscopy*, vol. 3, Wiley, New York, **1988**; Vol. p. 565.
- [17] W. H. Fuchsman, Q. R. Smith, M. M. Stein, *J. Am. Chem. Soc.* **1977**, *99*, 4190.
- [18] J. M. Burke, J. R. Kincaid, T. G. Spiro, *J. Am. Chem. Soc.* **1978**, *100*, 6077.
- [19] T. D. Brennan, W. R. Scheidt, *Acta Crystallogr. C* **1988**, *44*.
- [20] X.-Y. Li, R. S. Czernuszewicz, J. R. Kincaid, P. Stein, T. G. Spiro, *J. Phys. Chem.* **1990**, *94*, 47.
- [21] M. Abe, T. Kitagawa, K. Kyogoku, *J. Chem. Phys.* **1978**, *69*, 4526.
- [22] R. Puntharod, G. T. Webster, M. Asghari-Khiavi, K. R. Bambery, F. Safinejad, S. Rivadehi, S. J. Langford, K. J. Haller, B. R. Wood, *J. Phys. Chem. B* **2010**, *114*, 12104.
- [23] D. Truhlar, Y. Zhao, *J. Chem. Phys.* **2006**, *125*, 194101.
- [24] R. L. Martin, P. J. Hay, *J. Chem. Phys.* **1981**, *75*, 4539.
- [25] D. Avci, Y. Atalay, *Int. J. Quantum Chem.* **2009**, *109*, 328.
- [26] A. M. Amado, S. M. Fiuza, M. P. M. Marques, L. A. E. Batista de Carvalho, *J. Chem. Phys.* **2007**, *127*, 185104.
- [27] J. E. Falk, *Porphyrins and Metalloporphyrins-Their General, Physical and Coordination Chemistry, and Laboratory Methods*, vol. 2, Elsevier, Amsterdam, **1964**; Vol.
- [28] G. T. Webster, D. McNaughton, B. R. Wood, *J. Phys. Chem. B* **2009**, *113*, 6910.
- [29] M. E. Ali, P. M. Oppeneer, *Chem. A Eur. J.* **2015**, *21*, 8544.
- [30] H. N. Fonda, W. A. Oertling, A. Salehi, C. K. Chang, G. T. Babcock, *J. Am. Chem. Soc.* **1990**, *112*, 9497.
- [31] J. R. Kincaid, M. W. Urban, T. Watanabe, K. Nakamoto, *J. Phys. Chem.* **1983**, *87*, 3096.
- [32] T. Frosch, S. Koncarevic, L. Zedler, M. Schmitt, K. Schenzel, K. Becker, J. Popp, *J. Phys. Chem. B* **2007**, *111*, 11047.
- [33] T. Frosch, S. Koncarevic, K. Becker, J. Popp, *Analyst* **2009**, *134*, 1126.
- [34] K. Nakamoto, *Infrared and Raman Spectra of Inorganic and Coordination Compounds; Part B: Applications in Coordination, Organometallic, and Bioinorganic Chemistry*, 5th ed., Wiley, New York, **1997**.
- [35] T. Kitagawa, Y. Ozaki, *Struct. Bonding* **1997**, *64*, 73.
- [36] T. Uno, K. Hatano, Y. Nishimura, Y. Arata, *Inorg. Chem.* **1990**, *29*, 2803.
- [37] T. G. Spiro, J. M. Burke, *J. Am. Chem. Soc.* **1976**, *98*, 5482.
- [38] T. G. Spiro, R. S. Czernuszewicz, *Methods Enzymol.* **1995**, *246*, 416.
- [39] J. A. Shelnut, V. Ortiz, *J. Phys. Chem.* **1985**, *89*, 4733.
- [40] R. Puntharod, K. J. Haller, B. R. Wood, E. G. Robertson, **2009**, *Asian Crystallographic Association and the Chinese Crystallographic Society AsCA-2009*, Beijing, China. Abstract RS-9.

## Supporting information

Additional Supporting Information may be found online in the supporting information tab for this article.